# Mössbauer spectra as a "fingerprint" in tin–lithium compounds: Applications to Li-ion batteries

F. Robert[a],*, P.E. Lippens[a], J. Olivier-Fourcade[a], J.-C. Jumas[a], F. Gillot[b], M. Morcrette[b], J.-M. Tarascon[b]

[a]*Laboratoire des Agrégats Moléculaires et Matériaux Inorganiques (UMR 5072 CNRS), CC15, Université Montpellier II, Place Eugène Bataillon, 34095 Montpellier Cedex 5, France*
[b]*Laboratoire de Réactivité et Chimie des Solides (UMR 6007 CNRS), Université de Picardie Jules Verne, 33 rue Saint Leu, 80039 Amiens, France*

## Abstract

Several Li–Sn crystalline phases, i.e. $Li_2Sn_5$, LiSn, $Li_7Sn_3$, $Li_5Sn_2$, $Li_{13}Sn_5$, $Li_7Sn_2$ and $Li_{22}Sn_5$ were prepared by ball-milling and characterized by X-ray powder diffraction and $^{119}Sn$ Mössbauer spectroscopy. The analysis of the Mössbauer hyperfine parameters, i.e. isomer shift ($\delta$) and quadrupole splitting ($\Delta$), made it possible to define two types of Li–Sn compounds: the Sn-richest compounds ($Li_2Sn_5$, LiSn) and the Li-richest compounds ($Li_7Sn_3$, $Li_5Sn_2$, $Li_{13}Sn_5$, $Li_7Sn_2$, $Li_{22}Sn_5$). The isomer shift values ranged from 2.56 to 2.38 mm s$^{-1}$ for $Li_2Sn_5$, LiSn and from 2.07 to 1.83 mm s$^{-1}$ for $Li_7Sn_3$, $Li_5Sn_2$, $Li_{13}Sn_5$, $Li_7Sn_2$ and $Li_{22}Sn_5$, respectively. A $\Delta-\delta$ correlation diagram is introduced in order to identify the different phases observed during the electrochemical process of new Sn-based materials. This approach is illustrated by the identification of the phases obtained at the end of the first discharge of $\eta$-$Cu_6Sn_5$ and $SnB_{0.6}P_{0.4}O_{2.9}$.
© 2006 Elsevier Inc. All rights reserved.

*Keywords:* Li-ion batteries; Li–Sn alloys; Mössbauer spectroscopy

## 1. Introduction

The increasing demand for electric energy in many applications has lead to intensive research on batteries. Carbonaceous materials are commonly used as negative electrodes in commercial lithium-ion batteries [1–3]. Carbonaceous materials usually show good cycling performances and little volume change during the lithiation and de-lithiation cycles. However, the maximum theoretical specific capacity is only 372 mA h g$^{-1}$ corresponding to the formation of the $LiC_6$ graphite intercalation compound. Many intermetallic-based anode materials have been studied to increase the limited capacity and improve the cycling life of graphite [4,5]. Tin-based lithium storage materials are often referred to as alternative electrodes due to their reasonably low potentials for Li$^+$ insertion and high storage capacities [6–9]. Poor cyclability due to large volume changes occurring during lithium insertion and extraction is still a major problem, which is responsible for electrode disintegration. Previous papers pointed out that these limitations can be partly both overcome by reducing the metal particle size and using multi-phase systems or compounds [10–14]. Lithium extensively reacts with tin, up to the maximum stoichiometry of $Li_{22}Sn_5$ [15], corresponding to a specific capacity of 991 mA h g$^{-1}$ which is considerably higher than that of graphite and coke. However, the Li-insertion mechanism is mainly based on the formation of Li–Sn compounds leading to high volume changes of the particles during cycling. Therefore, reversibility is strongly limited. The volume of the highly lithiated compound, i.e. $Li_{22}Sn_5$, increases by 300% compared to $\beta$-Sn, which leads to the formation of microcracks within the electrode.

In order to solve these problems, several authors put forward composite materials in which an electrochemically

---

*Corresponding author. Fax: +33 4 67143304.
*E-mail address:* frobert@univ-montp2.fr (F. Robert).

inactive matrix acts as a buffer to reduce the effects of volume changes. Fuji Photo Film Co. announced a new type of anode materials [13,16] based on tin-composite oxide (TCO) glasses with significantly higher reversible specific ($> 600\,\text{mA h g}^{-1}$) and volumetric ($> 2200\,\text{mA h cm}^{-3}$) capacities. Sony recently released a tin-based amorphous anode material named Nexelion [17] in which the lithium ion storage capacity is 50% higher than that of carbonaceous materials, the overall battery capacity is thus increased by 30%. The mechanisms of the above-mentioned materials are complex. The result of the reactions is the formation of Li–Sn nano-compounds with distinct stoichiometries.

The purpose of this work is to introduce a method to identify the various Li–Sn compounds formed during electrochemical reactions ("fingerprint"). The binary diagram Li–Sn [18] shows the existence of 7 phases: $Li_2Sn_5$, LiSn, $Li_7Sn_3$ $Li_5Sn_2$, $Li_{13}Sn_5$, $Li_7Sn_2$ and $Li_{22}Sn_5$ whose structures were characterized by X-ray diffraction (XRD) [19–25]. The Li-richest phase is known to be $Li_{22}Sn_5$ according to the binary phase diagram, but recent studies revised its crystal structure and reported the $Li_{17}Sn_4$ stoichiometry [26–29]. These two compounds have close compositions, 4.25 Li/Sn for $Li_{17}Sn_4$ and 4.4 Li/Sn for $Li_{22}Sn_5$, and similar Sn local environments. Consequently, it is almost impossible to differentiate the Mössbauer parameters and we will not discuss the correct stoichiometry of the Li-richest phase in this paper. For simplicity, we consider $Li_{22}Sn_5$ as the Li-richest phase in this paper. The Li–Sn phases can be obtained by the following methods: (i) the syntheses by solid state reaction that do not allow us to obtain all Li–Sn pure phases [30] and to control the particles size, (ii) the electrochemical route which yields small quantities of materials [31], and (iii) the microwave-assisted solid-state reaction [29]. Here we used an alternative method, the mechanical alloying [32], which is a powerful technique to synthesize very different materials such as metallic to ionic extended solid solutions, compounds made up of immiscible elements or compounds made up of elements with very different melting point temperatures [33]. Furthermore, mechanosynthesis yields large amounts of rather pure Li–Sn compounds that can be used as references for Mössbauer experiments.

## 2. Experimental

The materials were obtained with an SPEX 8000 vibratory mill. The vial was shaken at frequency of 20 Hz in the three orthogonal directions. The impact speed of the balls was several $\text{m s}^{-1}$ and the shock frequencies were several hundred Hz. A pure Sn rod (99.9% Aldrich) and a Li foil (99.9% FMC) were used for the synthesis. The starting materials were put in stoichiometric amounts and were sealed into a stainless steel milling container ($25\,\text{cm}^3$) with stainless steel balls for 48 h under argon atmosphere. The experiments were performed in a glove box under argon atmosphere. The ball to powder weight ratio was 50:1. The mechanically alloyed powder was annealed into a

Table 1
Annealing temperature ($T_{an}$) used to synthesize the Li–Sn samples

| Compound | $T_{an}$ (°C) |
|---|---|
| $Li_2Sn_5$ | 150 |
| LiSn | 250 |
| $Li_7Sn_3$ | 400 |
| $Li_5Sn_2$ | 420 |
| $Li_{13}Sn_5$ | 400 |
| $Li_7Sn_2$ | 600 |
| $Li_{22}Sn_5$ | 150 |

sealed stainless steel tube in a vacuum furnace at a temperature ($T_{an}$) for 168 h (Table 1). The different annealing temperatures were selected from the Li–Sn binary diagram by considering a value lower than the melting or peritectic temperatures, to avoid crystalline growth.

The purity and crystallinity of the phases were examined by XRD using a D8 Brucker diffractometer (Co$K\alpha$ radiation source, $\theta-\theta$ geometry). Data gathering was performed for $2\theta$ angles ranging from $20°$ to $90°$. During the analysis, the powders were maintained in a hermetically closed aluminium sample holder with a beryllium window to prevent oxygen contamination.

The $^{119}$Sn Mössbauer spectra were recorded in transmission mode in the constant acceleration mode. The source used for this experiment was $^{119m}$Sn embedded in a CaSnO$_3$ matrix. The velocity scale was calibrated with the magnetic sextet of a high-purity iron foil as the reference absorber, and $^{57}$Co (Rh) was used as the source. The spectra were fitted to Lorentzian profiles by the least-squares method and the errors regarding the hyperfine parameters due to this method are found to be smaller than $0.01\,\text{mm s}^{-1}$ for the different Li–Sn compounds. Thus, the total error is estimated to be about $0.03\,\text{mm s}^{-1}$. The isomer shift values are given relative to the $\delta$ value of a BaSnO$_3$ spectrum recorded at room temperature. The absorbers containing $1–2\,\text{mg cm}^{-2}$ of $^{119}$Sn were prepared inside a glove box under argon atmosphere, by mixing the powder samples with Apiezon® vacuum grease between two Kapton® films. The sample holder was then sealed to prevent air contact.

Electrochemical tests were performed in Swagelok$^{TM}$-type cells assembled in an argon-filled glove box. Each cell was made up of a composite positive electrode containing the active material mixed with 10% acetylene black, a Li metal disc as the negative electrode, and a Whattman borosilicate glass microfibre separator with LiPF$_6$ (1 M) in PC/EC/DMC as the electrolyte. The discharge/charge curves were measured with a Mac Pile system operating in galvanostatic mode.

## 3. Results

The XRD patterns are shown in Fig. 1 and show the high crystallinity of our samples. The purity of LiSn,
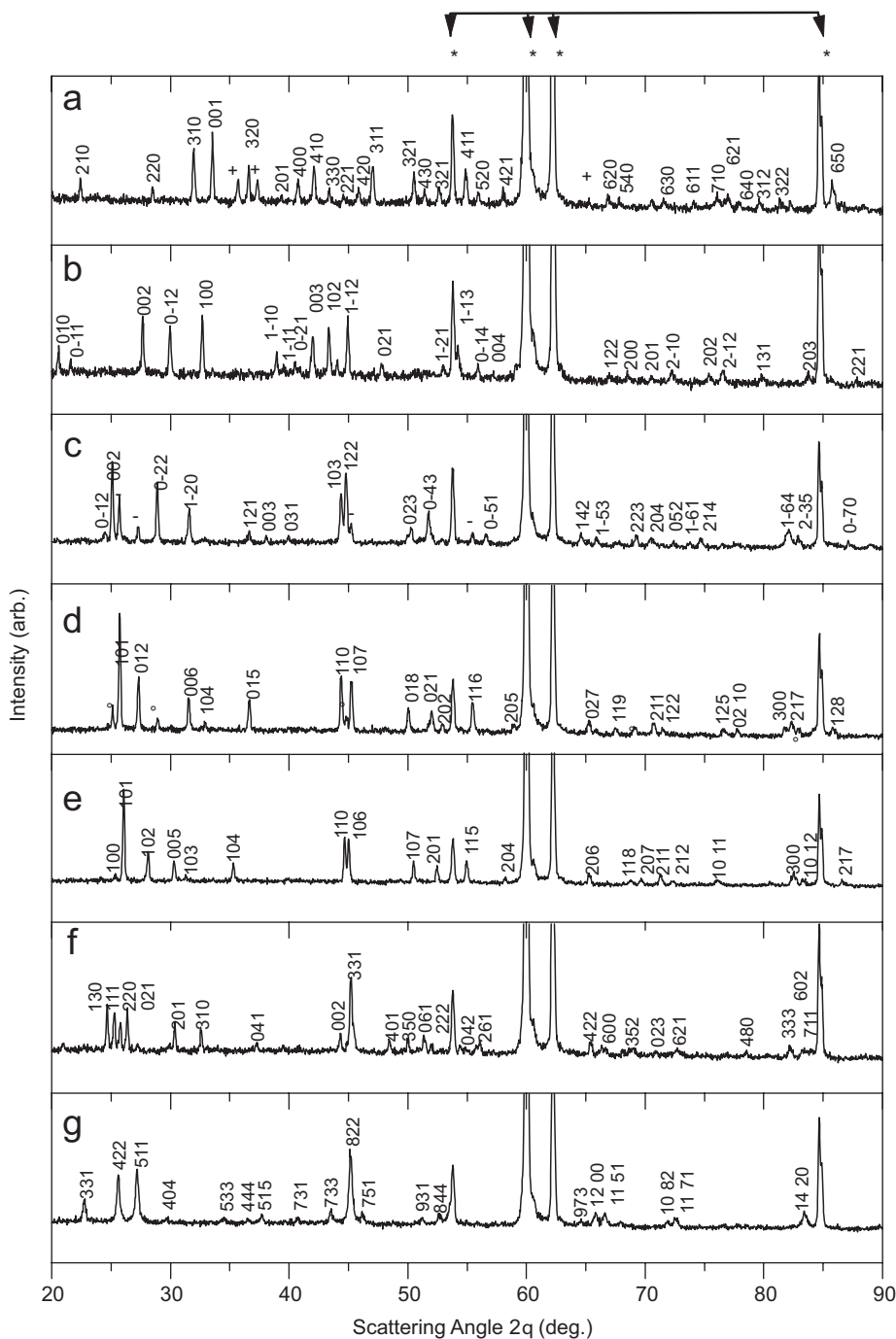
Fig. 1. XRD patterns of (a) $Li_2Sn_5$, (b) LiSn, (c) $Li_7Sn_3$, (d) $Li_5Sn_2$, (e) $Li_{13}Sn_5$, (f) $Li_7Sn_2$ and (g) $Li_{22}Sn_5$. [(*) beryllium of the sample holder, (+) $\beta$-Sn, (−) $Li_5Sn_2$, (°) $Li_7Sn_3$].

$Li_{13}Sn_5$, $Li_7Sn_2$ and $Li_{22}Sn_5$ was confirmed after comparison with the JCPDS database. The XRD pattern of the Sn-richest phase, $Li_2Sn_5$, shows the presence of $\beta$-Sn. As for the following three phases, $Li_7Sn_3$, $Li_5Sn_2$ and $Li_{13}Sn_5$, corresponding to small variations of the Li/Sn ratio (2.33; 2.5; 2.6, respectively) it was possible to obtain rather pure phases. Impurities were only detected for $Li_5Sn_2$ and $Li_7Sn_3$, $Li_7Sn_3$ contained some $Li_5Sn_2$ impurity and vice versa.

The data information is provided by Mössbauer Spectroscopy (MS) through the two hyperfine parameters: the isomer shift $\delta$, which is mainly related to the $s$ electron density (ED) at the Sn nucleus and the quadrupole splitting $\Delta$, which is related to the asymmetry of the electron distribution around the Sn atom. The Mössbauer spectra of the Li–Sn compounds recorded at room temperature are shown in Fig. 2. The spectra were fitted to Lorentzian peaks by taking into account the information obtained by
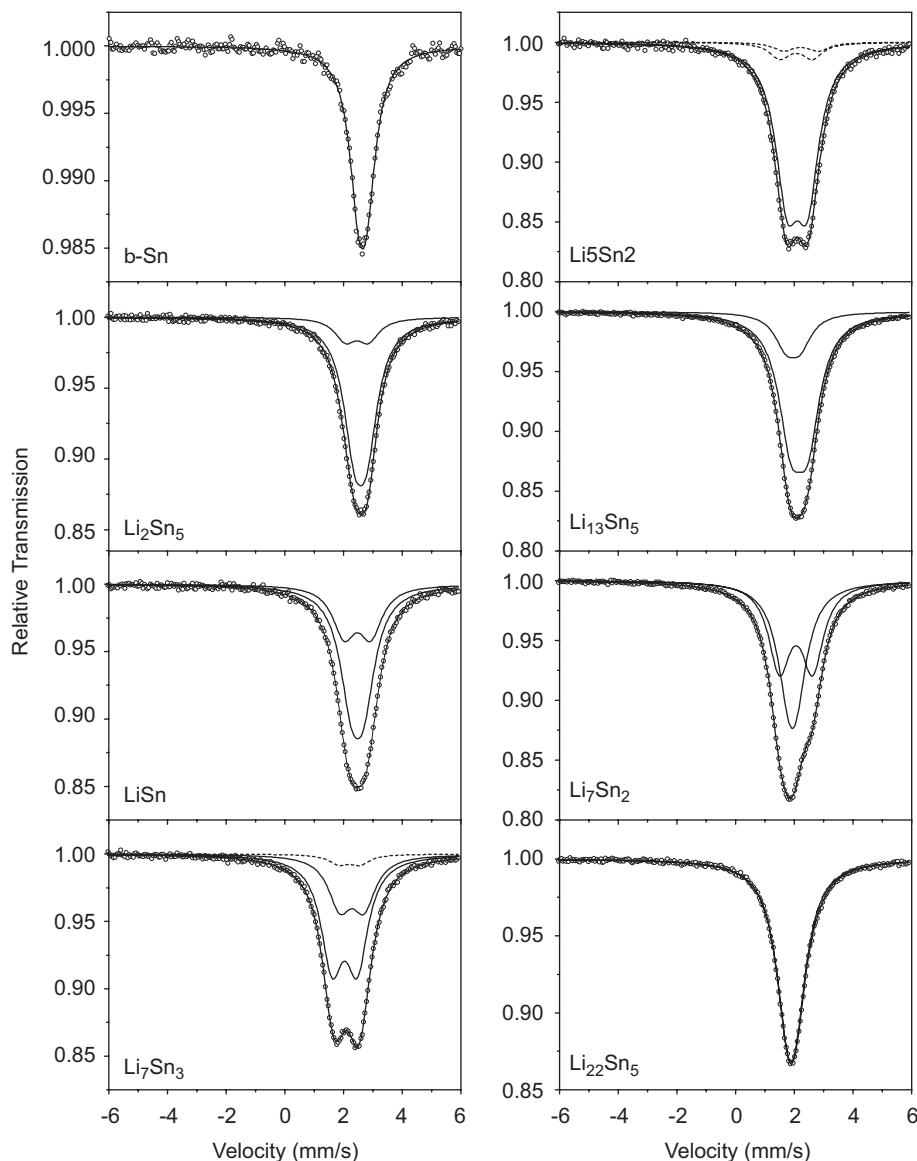
Fig. 2. $^{119}$Sn Mössbauer spectra of Li–Sn compounds at room temperature. The contributions of the main phases and impurities are shown by solid and dashed lines, respectively.
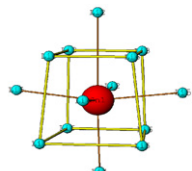
XRD: the different Sn crystallographic sites of the main phases and of the observed impurities. Only the relative contributions were set according to the relative number of Sn crystallographic sites (Table 2). The values of the hyperfine parameters can be found in Table 3. $Li_2Sn_5$ was fitted with two quadrupole doublets corresponding to the two nonequivalent Sn crystallographic sites of this compound (8$i$ and 2$d$, $P4/mbm$). Although $\beta$-Sn is observed by XRD, its contribution was omitted because of the small value of the recoil-free fraction at room temperature ($f \approx 0.04$ [34]). We verified the fact that taking into account a small component due to $\beta$-Sn does not affect the values of the hyperfine parameters of $Li_2Sn_5$. The LiSn spectrum was fitted with two quadrupole doublets in agreement with the crystallographic structure. It is important to note that the $\delta$ values of the two Sn crystallographic sites (1$a$ and 2$m$, $P2/m$) are equal: $\delta = 2.38 \, mm \, s^{-1}$. No other component is

needed to improve the fitting of the experimental data, which confirms the purity of the LiSn phase as observed by XRD. The $^{119}$Sn Mössbauer spectrum of $Li_7Sn_3$ consists of two quadrupole doublets corresponding to the two tin sites with similar symmetry (2$e$/2$e$, $P2_1/m$) but an additional small component (5%) was considered to take into account impurities. The $Li_5Sn_2$ spectrum was fitted with one quadrupole doublet to account for the only crystallographic site of this phase (6$c$, $R-3m$) and an impurity component formed by two quadrupole doublets, corresponding to $Li_7Sn_3$ (13%). The spectrum of $Li_{13}Sn_5$ was fitted with two quadrupole doublets only since two out of the three tin crystallographic sites have similar environments (1$a$ and 2$d$/2$d$, $P-3m1$). The spectrum of $Li_7Sn_2$ was fitted with two quadrupole doublets to account for the two types of Sn crystallographic sites (4$i$ and 4$h$, $Cmmm$) of this structure. The spectrum of $Li_{22}Sn_5$ was fitted with only one

Table 2
Main structural features of the Li–Sn phases

| Compound | N | Site designation | Sn local environment | | Average bond lengths (Å) | | ED |
|---|---|---|---|---|---|---|---|
| | | | | | Sn–X | In first polyhedron | |
| *First polyhedron*: $[6 + X]\,0 \leqslant X \leqslant 6$ | | | | | | | |
| β-Sn | 1 | 4a | [4Sn + 2Sn] | $Sn_1$–4Sn | 3.02 (2) | 3.07 | 4.00 |
| | | | | $Sn_1$–2Sn | 3.18 (1) | | |
| Li₂Sn₅ | 2 | 8i | [5Sn + 1Sn + 4Li] | $Sn_1$–5Sn | 3.13 (2) | 3.16 | 3.14 |
| | | | | $Sn_1$–4Li | 3.16 (3) | | |
| | | | | $Sn_1$–Sn | 3.31 (1) | | |
| | | 2d | [6Sn + 4Li] | $Sn_2$–4Li | 2.92 (1) | 3.04 | |
| | | | | $Sn_2$–6Sn | 3.12 (3) | | |
| | 2 | 1a | [8Li + 4Sn] | $Sn_1$–8Li | 3.04 (4) | 3.07 | 2.50 |
| | | | | $Sn_1$–3Sn | 3.12 (3) | | |
| | | | | $Sn_1$–Sn | 3.16 (2) | | |
| | | 2m | | $Sn_2$–8Li | 3.05 (2) | 3.09 | |
| LiSn | | | | $Sn_2$–4Sn | 3.17 (1) | | |
| *First polyhedron*: [8 + 6] | | | | | | | |
| | 1 | 2e | [2Sn + 6Li] + 6Li | $Sn_1$–6Li | 2.93 (2) | 3.09 | 1.90 |
| | | | | $Sn_1$–2Sn | 2.94 (1) | | |
| | | | | $Sn_1$–6Li | 3.29 (2) | | |
| | + | 2e | [1Sn + 7Li] + 6Li | $Sn_2$–7Li | 2.85 (6) | 3.05 | |
| | | | | $Sn_2$–Sn | 2.94 (1) | | |
| | | | | $Sn_2$–6Li | 3.31 (5) | | |
| Li₇Sn₃ | 2 | 2e | [1Sn + 7Li] + 6Li | $Sn_3$–7Li | 2.85 (6) | 3.07 | |
| | | | | $Sn_3$–Sn | 2.94 (1) | | |
| | | | | $Sn_3$–6Li | 3.34 (5) | | |
| | 1 | 6c | [1Sn + 7Li] + 6Li | $Sn_1$–Li | 2.72 (1) | 3.07 | 1.86 |
| | | | | $Sn_1$–Sn | 2.88 (1) | | |
| Li₅Sn₂ | | | | $Sn_1$–6Li | 2.93 (2) | | |
| | | | | $Sn_1$–6Li | 3.30 (2) | | |
| | 1 | 1a | [8Li] + 6Li | $Sn_1$–8Li | 2.87 (6) | 3.08 | 1.83 |
| | | | | $Sn_1$–6Li | 3.37 (2) | | |
| | + | 2d | [1Sn + 7Li] + 6Li | $Sn_2$–Sn | 2.86 (2) | 3.06 | |
| | | | | $Sn_2$–7Li | 2.89 (3) | | |
| | | | | $Sn_2$–6Li | 3.28 (2) | | |
| | 2 | 2d | [1Sn + 7Li] + 6Li | $Sn_3$–Sn | 2.86 (5) | | |
| Li₁₃Sn₅ | | | | $Sn_3$–7Li | 2.87 (2) | | |
| | | | | $Sn_3$–6Li | 3.28 (3) | | |

Table 2 (*continued*)

| Compound | N | Site designation | Sn local environment | | Average bond lengths (Å) | | ED |
|---|---|---|---|---|---|---|---|
| | | | | | Sn–X | In first polyhedron | |
| *First polyhedron* [14] | | | | | | | |
| | 1 | 4i | [8Li + 4Li] + 2Li | Sn$_1$–8Li | 2.86 (2) | 3.01 | 1.66 |
| | | | | Sn$_1$–4Li | 3.05 (4) | | |
| | | | | Sn$_1$–2Li | 3.51 (1) | | |
| | + | 4h | 1Sn + 6Li + 2Li + 5Li | Sn$_2$–6Li | 2.89 (5) | 3.06 | |
| | | | | Sn$_2$–Sn | 2.99 (2) | | |
| | | | | Sn$_2$–2Li | 3.12 (4) | | |
| Li$_7$Sn$_2$ | | | | Sn$_2$–5Li | 3.24 (8) | | |
| | 4 | 16e | 8Li + 6Li | Sn$_1$–8Li | 2.86 (9) | 3.05 | 1.55 |
| | | | | Sn$_1$–6Li | 3.30 (5) | | |
| | | 16e | 8Li + 6Li | Sn$_2$–8Li | 2.86 (9) | 3.05 | |
| | | | | Sn$_2$–8Li | 3.30 (5) | | |
| | | 24f | 4Li + 5Li + 5Li | Sn$_3$–4Li | 2.72 (1) | 3.05 | |
| | | | | Sn$_3$–5Li | 3.01 (4) | | |
| Li$_{22}$Sn$_5$ | | | | Sn$_3$–5Li | 3.36 (9) | | |
| | | 24g | 4Li + 5Li + 5Li | Sn$_4$–4Li | 2.72 (1) | 3.05 | |
| | | | | Sn$_4$–5Li | 3.01 (3) | | |
| | | | | Sn$_4$–5Li | 3.36 (9) | | |

The numbers in brackets denote the number of Sn neighbours in the Sn-centred first polyhedron including both short and long bond lengths. *N* denotes the number of Sn crystallographic sites and ED the electron density calculated from the Hume–Rothery rule [37].

Table 3
Hyperfine parameters obtained from $^{119}$Sn Mössbauer spectra at room temperature

| Compound | Site, impurities | $\delta$ (mm s$^{-1}$) | $\bar{\delta}$ (mm s$^{-1}$) | $\Delta$ (mm s$^{-1}$) | $\Gamma$ (mm s$^{-1}$) | $I$ (%) | |
|---|---|---|---|---|---|---|---|
| $\beta$-Sn | 4a | 2.56 | 2.56 | 0.29 | 0.91 | 100 | |
| Li$_2$Sn$_5$ | 8i | 2.49 | 2.46 | 0.42 | 0.93 | 80 | |
| | 2d | 2.36 | | 0.78 | 0.92 | 20 | |
| LiSn | 2m | 2.38 | 2.38 | 0.43 | 0.93 | 67 | |
| | 1a | 2.38 | | 0.91 | 0.95 | 33 | |
| Li$_7$Sn$_3$ | 2e | 2.19 | 2.02 | 0.82 | 0.95 | 31 | |
| | 2e/2e | 1.94 | | 0.86 | 0.90 | 64 | |
| | Li$_5$Sn$_2$ | 2.07 | 2.07 | 0.72 | 0.88 | 5.2 | |
| Li$_5$Sn$_2$ | 6c | 2.01 | 2.01 | 0.69 | 0.94 | 87 | |
| | Li$_7$Sn$_3$ 2e | 2.14 | 2.02 | 1.2 | 0.86 | 5 | 13 |
| | Li$_7$Sn$_3$ 2e/2e | 1.96 | | 1.12 | 0.87 | 8 | |
| Li$_{13}$Sn$_5$ | 1a | 1.86 | 2 | 0.48 | 0.93 | 20 | |
| | 2d/2d | 2.07 | | 0.58 | 0.96 | 80 | |
| Li$_7$Sn$_2$ | 4i | 1.84 | 1.9 | 0.28 | 0.96 | 50 | |
| | 4h | 1.96 | | 1.13 | 0.89 | 50 | |
| Li$_{22}$Sn$_5$ | 16e/16e/24f/24g | 1.83 | 1.83 | 0.31 | 0.97 | 100 | |
| $\eta$-Cu$_6$Sn$_5$ end discharge | | 1.87 | 1.91 | 0.28 | 0.89 | 64 | |
| | | 1.95 | | 0.98 | 0.91 | 36 | |
| SnB$_{0.6}$P$_{0.4}$O$_{2.9}$ end discharge | | 2.03 | 2.035 | 0.55 | 0.87 | 53 | |
| | | 2.04 | | 1.49 | 0.87 | 47 | |

Sn crystallographic sites and impurities considered in the Mössbauer fitting procedure, isomer shift $\delta$ relative to BaSnO3, average isomer shift $\bar{\delta}$, quadrupole splitting $\Delta$, line width at half-maximum $\Gamma$ and relative areas of the sub-spectra $I$. The error on the hyperfine parameters is about 0.03 mm s$^{-1}$.

unresolved quadrupole doublet because the four Sn crystallographic sites show hardly differ from each other as far as symmetry is concerned ($16e/16e/24f/24g$, $Im–3m$).

## 4. Discussion

The structural data of the Li–Sn phases [18–25] are summarized in Table 2, and their structures, as reported by Chouvin et al. [35] can be found in Fig. 3.

Both the Sn-richest phase ($Li_2Sn_5$), based on tin stacking, and the Li-richest phase ($Li_{22}Sn_5$), based on lithium stacking, have three-dimensional lattices whereas the other phases have two-dimensional lattices (Fig. 3). The Sn-richest compound, $Li_2Sn_5$, is made up of a three-dimensional tin network with channels partly occupied by lithium atoms. LiSn is a two-dimensional structure built on alternate layers of tin and lithium atoms. In $Li_7Sn_3$, $Li_5Sn_2$, $Li_{13}Sn_5$ and $Li_7Sn_2$, the layers mainly contain lithium atoms; diatomic ($Li_{13}Sn_5$ and $Li_7Sn_2$) and triatomic ($Li_7Sn_3$) arrangements of tin atoms inside or tin isolated in different proportions for $Li_{13}Sn_5$ and $Li_7Sn_2$. In these phases the Sn–Sn bond lengths are short and the Li–Sn bonds are divided into two groups involving the first nearest neighbours ($<3$ Å) and the second nearest neighbours ($3$ Å $< d < 3.30$ Å), respectively. The value of $3.30$ Å is regarded as the limit length because it defines the standard coordination of the Sn-centred polyhedra [36]. $Li_{22}Sn_5$, which is the Li-richest compound, has a three-dimensional structure based on a network of lithium atoms in which tin occupies the cubic sites. In this structure, there are no strong Sn–Sn interactions.

Since the purpose of this work is to characterize the phases from $^{119}$Sn hyperfine parameters, it is interesting to relate these structures to tin coordination. The evolution of the Li–Sn crystal structures shows a large variety of local atomic arrangements around the tin atoms. Two types of Sn-centred polyhedra can be distinguished: the Sn octahedral environments in the Sn-rich phases and the Sn cubic environments in the Li-rich phases. As far as the Sn-rich phases are concerned, the average number of Sn neighbours in the first Sn-centred polyhedron decreases from 6 to 4 as the number of Li neighbours increases. The decrease in the number of Sn neigbours and the increase in the bonding covalency have a strong influence on the dimensionality of the network. As for the Li-rich phases, the tin atoms are isolated or form small clusters with 2 or 3 atoms. The Sn–Sn bonds are covalent but do not modify the compact stacking based on the lithium atoms.

All these compounds can be characterized from the "ED" defined by Hume–Rothery as the ratio between the total number of valence electrons and the number of atoms in the unit cell [37]. The values of ED are reported in Table 2. They significantly decrease for Sn-rich phases because the Sn neighbours in the first polyhedron decrease. Fig. 4a shows the variations of the average value $\bar{\delta}$ as a function of ED. Two distinct ranges can be observed depending on the composition: (I) Sn-rich phases ($\beta$-Sn,

$Li_2Sn_5$, LiSn) and (II) Li-rich phases ($Li_7Sn_3$ $Li_5Sn_2$ $Li_{13}Sn_5$, $Li_7Sn_2$ and $Li_{22}Sn_5$). In region I, the $\bar{\delta}$ linearly decreases from 2.56 to 2.38 mm s$^{-1}$ with decreasing ED. The small slope 0.12 mm s$^{-1}$ can be correlated with the decrease in the number of Sn neighbours in the Sn-centred polyhedron (Table 3). In region II, the Li-rich phases present smaller $\bar{\delta}$ values, which decrease with a large slope of 0.56 mm s$^{-1}$ from 2.07 to 1.83 mm s$^{-1}$ as ED decreases.

Fig. 4b shows the change in $\bar{\delta}$ as a function of Li content. The values obtained by Dunlap et al. [30] are also shown for comparison and agree reasonably well with the values determined herein. This agreement indicates that both solid state reactions and ball milling yield similar compounds with the same Mössbauer spectral parameters. However, the latter approach yields large amounts of materials and avoids the high reaction temperatures and special containers required by the corrosive nature of the molten Li. Only the microwave-assisted solid-state reaction yields obtaining pure $Li_{17}Sn_4$ [29] and its hyperfine parameters are similar to those obtained herein for $Li_{22}Sn_5$, in agreement with the similar compositions of these two phases. The comparison of Figs. 4a and b indicates that the changes in $\bar{\delta}$ as a function of ED and Li content exhibit similar trends. Thus, $\bar{\delta}$ is a good indicator of the composition of the Li–Sn compounds and can be used to identify the phases occurring at the various stages of the electrochemical cycle.

If the isomer shift is an indicator of the structural type of the Li–Sn sample, the quadrupole splitting is directly related to the arrangement and nature of the neighbours of the Sn atoms during the electrochemical cycles. The correlation between the quadrupole splitting and the isomer shift for each Sn crystallographic site in the Li–Sn phases is shown in Fig. 5. From this correlation diagram it is possible to define some domains for the Sn- or Li-rich environments. It is worth noticing that the $\Delta$ values of the Sn-rich environments are less scattered than those of the Li-rich environments. The variations in the $\Delta$ values are mainly due to changes in the Sn local asymmetry that are related to the Li/Sn ratio.

In conclusion, the changes in $\bar{\delta}$ have been related to those in ED which are mainly dependant on the nature of the Sn first neighbours whereas the variations of $\Delta$ are mainly related to the Sn atomic coordination. The $\Delta-\delta$ correlation diagram represented in Fig. 5 could be useful to identify the nature of the Li–Sn compounds formed during the electrochemical reactions of new Sn-based electrode materials.

## 5. Applications of the $\Delta-\delta$ correlation diagram

It is possible to determine from Fig. 5 the stoichiometry of the Li–Sn phases formed during the electrochemical process. The exact composition of $Li_xSn$, is often difficult to characterize from XRD since the phases obtained by electrochemical reactions with lithium are amorphous and/or nano-crystallized. In this case, the use of $^{119}$Sn MS can greatly help in determining the phase composition, for
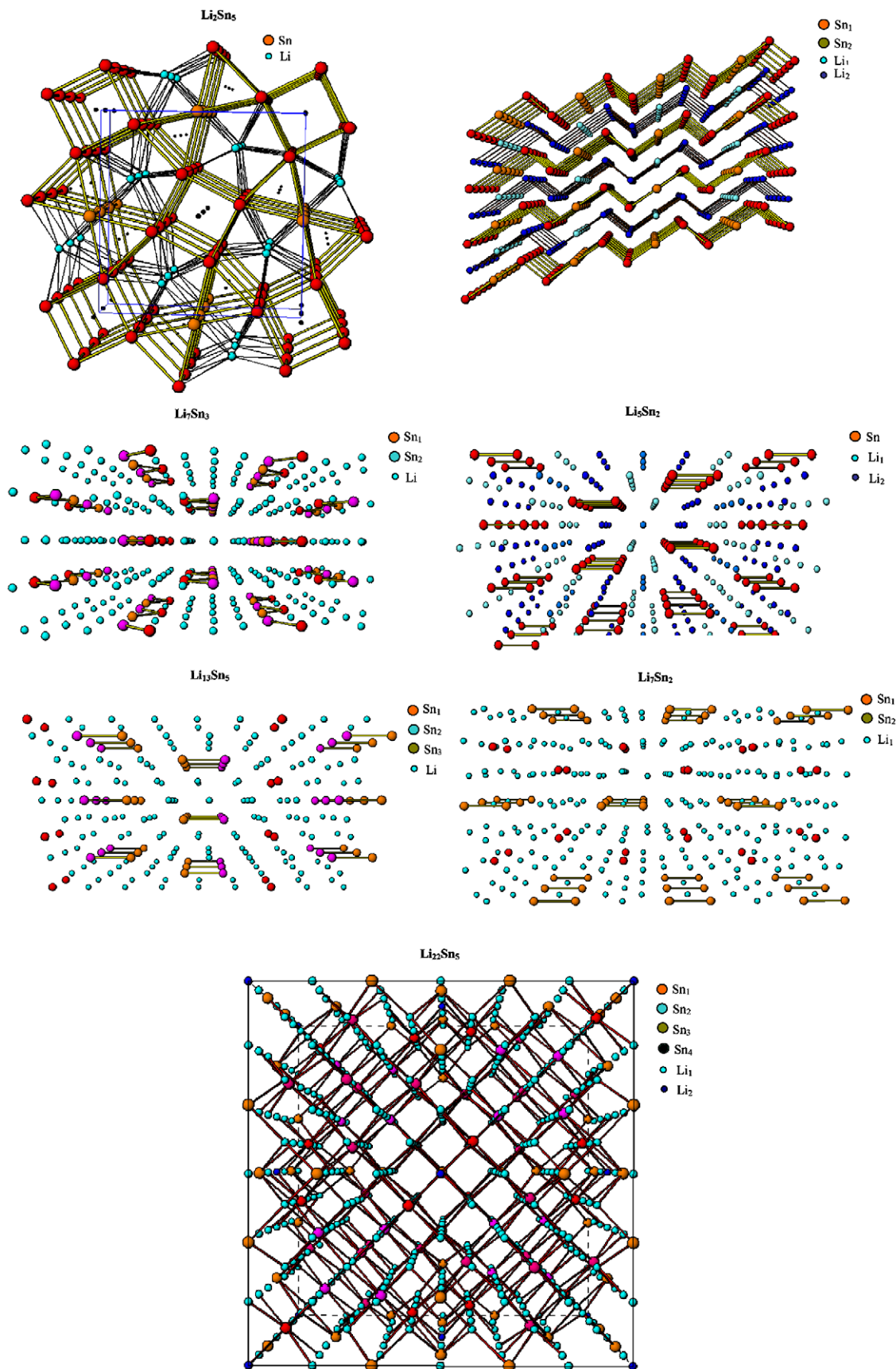
Fig. 3. Crystal structure representation of the different Li–Sn phases according to Chouvin et al. [29].
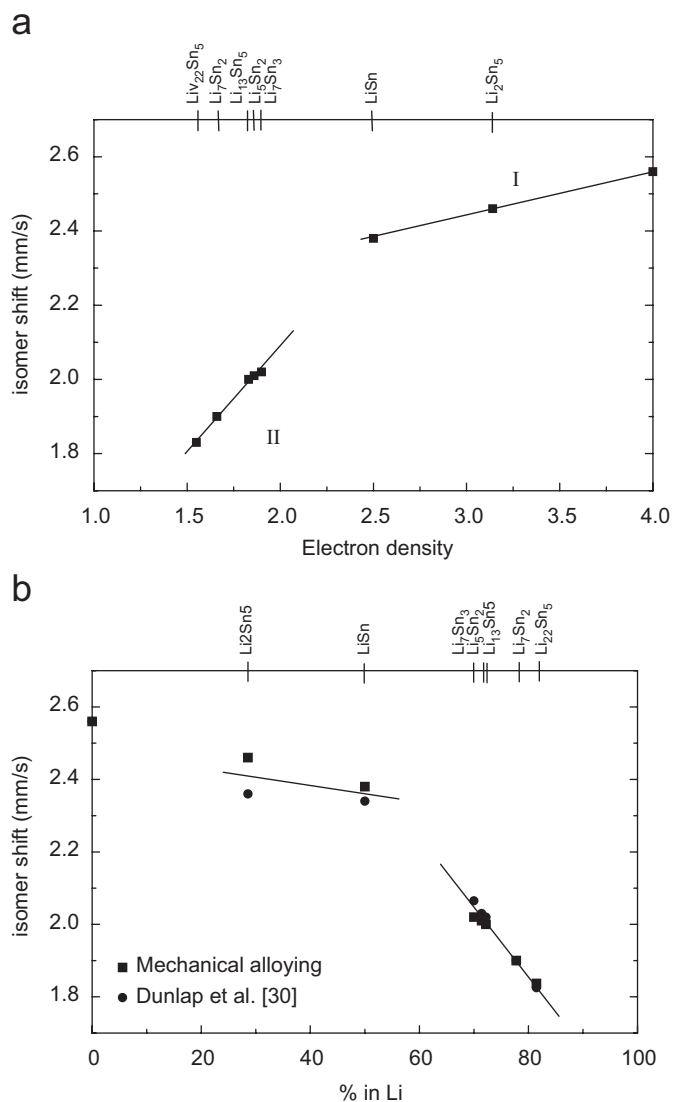
Fig. 4. (a) Average value of the isomer shift $\bar{\delta}$ (■) as a function of the electron density given in Table 3, (b) variations of $\bar{\delta}$ (■) as a function of the Li content for the Li–Sn compounds. The values obtained by Dunlap et al. (●) [30] are shown for comparison.



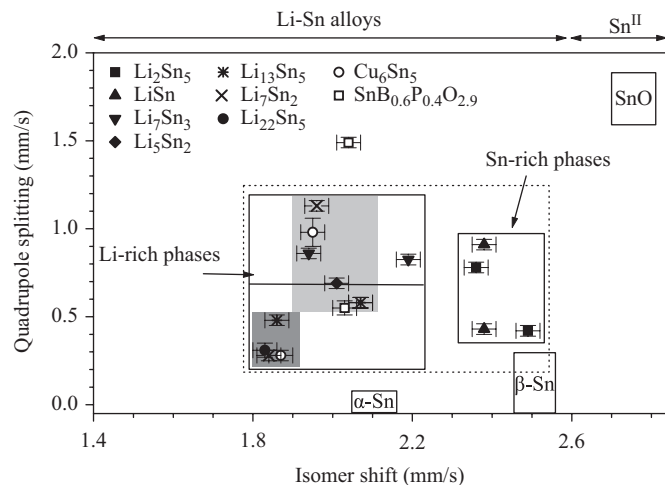Fig. 5. $\Delta$–$\delta$ correlation diagram for the different tin sites of the Li–Sn compounds. The symbols denote the different Li–Sn phases and the products obtained at the end of the discharge of $\eta$-$Cu_6Sn_5$ and $SnB_{0.6}P_{0.4}O_{2.9}$. The grey and the light-grey areas show Sn-centred polyhedra without and with one Sn first-nearest neighbours, respectively.
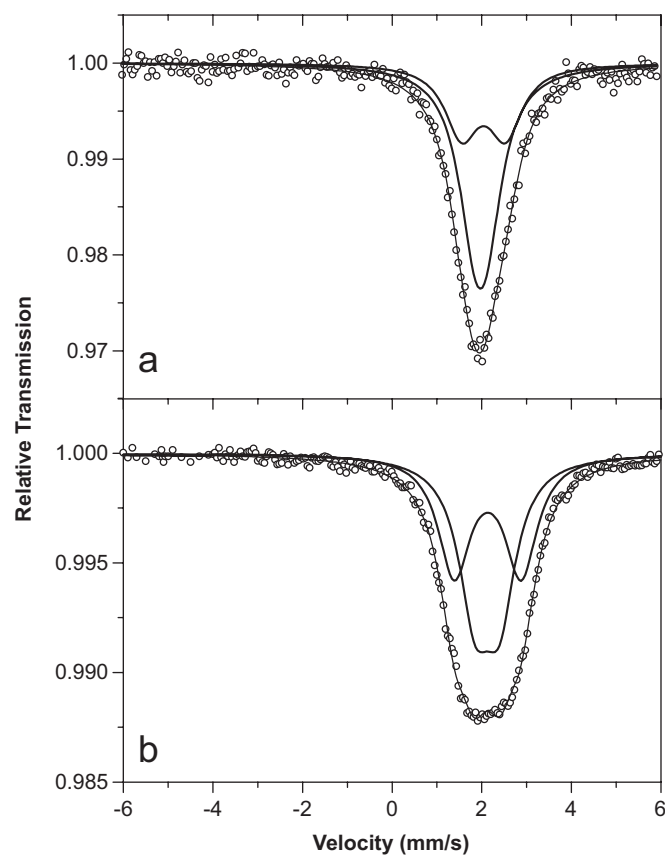


Fig. 6. $^{119}$Sn Mössbauer spectra at end of the first discharge for $\eta$-$Cu_6Sn_5$ (a) and $SnB_{0.6}P_{0.4}O_{2.9}$ (b).

example, $Li_{22}Sn_5$ and $Li_7Sn_2$. The spectra of two fully lithiated samples (at the end of the first discharge) are shown in Fig. 6 for $\eta$-$Cu_6Sn_5$ [38] and for $SnB_{0.6}P_{0.4}O_{2.9}$ composite glass [39]. It is usually acknowledged that $Li_{22}Sn_5$ is formed if all Li atoms have reacted with the electrode at 0.01 V since it is the highest electrochemically lithiated Li–Sn phase. For $\eta$-$Cu_6Sn_5$, both $Li_{22}Sn_5$ [40] and $Li_7Sn_2$ [41] were proposed as materials formed at the end of the discharge.

The Mössbauer parameters of the fully lithiated samples are reported in Table 3 and can be analysed from the $\Delta$–$\delta$ correlation diagram of Fig. 5. In the case of $\eta$-$Cu_6Sn_5$, the two Mössbauer parameters, $\delta$ and $\Delta$, are close to those of $Li_7Sn_2$ but not to those of $Li_{22}Sn_5$. For $SnB_{0.6}P_{0.4}O_{2.9}$, the $\delta$ and $\Delta$ values suggest a Li-rich phase with a composition between $Li_5Sn_2$ and $Li_{13}Sn_5$. The high values of $\Delta$ reveal the presence of a very distorted environment of tin atoms in

this compound, which could be explained by the presence of interactions between tin and oxygen atoms until the end of discharge, as previously described in SnO [42,43].

We can conclude by saying that $Li_7Sn_2$ was found to be the highest electrochemically lithiated phase at the end of

the $\eta$-$Cu_6Sn_5$ discharge whereas Li reacts with $SnB_{0.6}P_{0.4}O_{2.9}$ to form distinct Li-rich phases inside the composite electrode.

## 6. Conclusion

Pure Li–Sn crystalline phases were obtained by ball-milling method. Successful syntheses made the characterization of these phases with [119]Sn MS possible. The analysis of the isomer shift and quadrupole splitting in terms of crystal structure and ED as defined by Hume–Rothery allowed us to characterize two types of Li–Sn compounds : the Sn-richest compounds ($Li_2Sn_5$, LiSn) and the Li-richest compounds ($Li_7Sn_3$, $Li_5Sn_2$, $Li_{13}Sn_5$, $Li_7Sn_2$, $Li_{22}Sn_5$). From these results a $\Delta - \delta$ correlation diagram was generated and used to identify the Li–Sn phases during the electrochemical process of new Sn-based materials. Such an approach showed the presence of $Li_7Sn_2$ and Li-rich phases between $Li_5Sn_2$ and $Li_{13}Sn_5$ at the end of the first discharge of $\eta$-$Cu_6Sn_5$ and $SnB_{0.6}P_{0.4}O_{2.9}$, respectively.

## Acknowledgments

## References

[1] T. Nagaura, K. Tazawa, Prog. Batteries Solar Cells 9 (1990) 209.
[2] F.S. Disma, L. Aymard, L. Dupond, J.M. Tarascon, J. Electrochem. Soc. 143 (1996) 3959.
[3] F.S. Disma, C. Lenain, B. Beaudoin, L. Aymard, J.M. Tarascon, Solid State Ionics 98 (1997) 145.
[4] J. Yang, Y. Takeda, N. Imanishi, J.Y. Xie, O. Yamamoto, Solid State Ionics 96 (2000) 77.
[5] J.O. Besenhard, J. Yang, M. Winter, J. Power Sources 68 (1) (1997) 87.
[6] I.A. Courtney, J.R. Dahn, J. Electrochem. Soc. 144 (1997) 2045–2052.
[7] A.H. Whitehead, J.M. Elliott, J.R. Owen, J. Power Sources 81 (1999) 33–38.
[8] A.S. Yu, R. Frech, J. Power Sources 104 (2002) 97–100.
[9] Y.N. Nuli, S.L. Zhao, Q.Z. Qin, J. Power Sources 114 (2003) 113–120.
[10] T. Brousse, R. Retoux, U. Herterich, D.M. Schleich, J. Electrochem. Soc. 145 (1) (1998) 1.
[11] I.A. Courtney, J.R. Dahn, J. Electrochem. Soc. 144 (1997) 2943.
[12] M. Winter, J.O. Besenhard, M.E. Spahr, P. Novak, Adv. Mater. 10 (10) (1998) 725.
[13] Y. Idota, T. Kubota, A. Matsufuji, Y. Maekawa, T. Miyasaka, Science 276 (1997) 1395.
[14] P.E. Lippens, J. Olivier-Fourcade, J.C. Jumas, Hyperfine Interact. 126 (2000) 137.
[15] J. Wang, I.D. Raistrick, R.A. Huggins, J. Electrochem. Soc. 133 (1986) 457.
[16] Fuji Photo Film Co. Ltd., European Patent, EP 0704 921 A1, 1995.
[17] H. Tanizaki, Miyagi, A. Omaru, Fukushima, US Patent 2004/ 0053131 A1 (2004).
[18] C.J. Wen, R.A. Huggins, J. Electrochem. Soc. 128 (1981) 1181.
[19] D.A. Hansen, L.J. Chang, Acta Crystallogr. B 25 (1969) 2392.
[20] W. Müller, H. Schäfer, Z. Naturforsch. 28b (1973) 246.
[21] W. Müller, Z. Naturforsch. 29b (1974) 304.
[22] U. Frank, W. Müller, H. Schäfer, Z. Naturforsch. 30b (1975) 1.
[23] U. Frank, W. Müller, Z. Naturforsch. 30b (1975) 316.
[24] U. Frank, W. Müller, H. Schäfer, Z. Naturforsch. 30b (1975) 6.
[25] E.I. Gladyshevski, G.I. Oleksiv, P.I. Kripyakevich, Kristallografiya 9 (1964) 338;
   Sov. Phys. Crystallogr. 9 (1964) 269.
[26] R. Nesper, H.G. Schnering, J. Solid State Chem. 70 (1987) 48.
[27] G.R. Goward, N.J. Taylor, D.C.S. Souza, L.F. Nazar, J. Alloys Compds. 329 (2001) 82.
[28] C. Lupu, J.-G. Mao, J. Wayne Rabalais, A.M. Guloy, Inorg. Chem. 42 (2003) 3765.
[29] G.-T. Zhou, O. Palchik, I. Nowik, R. Herber, Y. Koltypin, A. Gedanken, J. Solid State Chem. 177 (2004) 3014.
[30] R.A. Dunlap, D.A. Small, D.D. MacNeil, M.N. Obravac, J.R. Dahn, J. Alloys Compds. 289 (1999) 135.
[31] J. Chouvin, J. Olivier-Fourcade, J.C. Jumas, B. Simon, O. Godiveau, Chem. Phys. Lett. 308 (1999) 413.
[32] E. Gaffet, F. Bernard, J.-C. Niepce, F. Charlot, C. Gras, G. Le Caër, J.-L. Guichard, P. Delcroix, A. Mocellin, O. Tillemet, J. Mater. Chem. 9 (1999) 305.
[33] Proceedings of the International Symposium on Metastable, Mechanically Alloyed and Nanocrystalline Materials (ISMANAM), Mater. Sci. Forum, 179–181 (1995); 225–227 (1996); 235–238 (1997); 269–272 (1998).
[34] A.A. Bahgat, Phys. Stat. Sol. B 97 (1980) K129.
[35] J. Chouvin, Ph.D. Thesis, Montpellier, 2001.
[36] M. Van Meersche, J. Feneau-Dupont, Introduction à la Cristallographie et à la Chimie Structurale, Vander, 1973.
[37] W. Hume–Rothery, H.M. Powell, Z. Kristallogr. 91 (1935) 23.
[38] S. Naille, unpublished results, private communication.
[39] J. Chouvin, C. Pérez Vicente, J. Olivier-Fourcade, J.-C. Jumas, B. Simon, P. Biensan, Solid State Sci. 6 (2004) 39.
[40] L. Fransson, E. Nordström, K. Edström, L. Häggström, J.T. Vaughey, M.M. Thackeray, J. Electrochem. Soc. 149 (6) (2002) A736.
[41] W. Choi, J.Y. Lee, H.S. Lim, Electrochem. Commun. 6 (2004) 816.
[42] J. Chouvin, J. Olivier-Fourcade, J.-C. Jumas, B. Simon, P. Biensan, F.J. Fernández Madrigal, J.L. Tirado, C. Pérez Vicente, J. Electroanal. Chem. 494 (2000) 136.
[43] F. Robert, F. Morato, J. Chouvin, L. Aldon, P.E. Lippens, J. Olivier-Fourcade, J.-C. Jumas, J. Power Sources 119–121 (2003) 581–584.